Hydrodynamics and gas transfer performance of confined hollow fibre membrane modules with the aid of computational fluid dynamics

Fatemeh Kavousi[a], Eoin Syron[a,b], Michael Semmens[c], Eoin Casey[a]*

[a] *School of Chemical and Bioprocess Engineering, University College Dublin (UCD),Belfield, Dublin 4, Ireland.*

[b] *OxyMem, Blyry, Athlone, Ireland*

[c] *Department of Civil, Environmental, and Geo- Engineering, University of Minnesota, USA*

* Corresponding author. Tel.: +353 1 716 1877. E-mail address: eoin.casey@ucd.ie (E. Casey)

Abstract

The use of gas permeable membranes for bubbleless aeration is of increasing interest due to the energy savings it affords in wastewater treatment applications. However, flow maldistributions are a major factor in the impedance of mass transfer efficiency. In this study, the effect of module configuration on the hydrodynamic conditions and gas transfer properties of various submerged hollow fibre bundles was investigated. Flow patterns and velocity profiles within fibre bundles were predicted numerically using computational fluid dynamics (CFD) and the model was validated by tracer-response experiments. In addition, the effect of fibre spacing and bundle size on the aeration rate of various modules was evaluated experimentally. Previous studies typically base performance evaluations on the liquid inlet velocity or an average velocity, an approach which neglects the effect of geometric features within modules. The use of validated CFD simulations provides more detailed information for performance assessment. It was shown that specific oxygen transfer rates declines significantly with increasing numbers of fibres in a bundle. However, the same trend was not observed when the fibre spacing is increased. A correlation was proposed for the prediction of the overall mass transfer coefficient utilizing the local velocity values obtained from the validated CFD model.

Keywords: Membrane aeration, Computational Fluid Dynamics (CFD), Hollow fiber module configuration, Mass transfer efficiency, Hydrodynamics

1. Introduction

Hollow fibre gas-liquid contact membranes are of increasing interest in a wide variety of applications including wastewater treatment, medical devices, and de-gassing of process industry liquid streams. The use of such contactors as bubble-less aeration devices in water/wastewater treatment has been under investigation for several years [1–10]. Enhancing the oxygen transfer rate to the liquid is of critical importance in these processes. High rates of mass transfer, close to 100% transfer efficiency [4], good process control and ability to operate at flow rates and pressure independent of the bulk fluid phase are some of the reasons for their superiority over energy intensive bubble aeration systems [8]. A commonly used membrane material in these applications is Polydimethylsiloxane (PDMS), due to its high oxygen permeability and robustness sin the wastewater milieu. The dense or non-porous nature of PDMS eliminates the possibility of bubble formation above moderate pressures and additionally prevents intra-pore fouling and wetting, which are disadvantages of porous membranes in these applications.

The rate of aeration is largely dependent on the effective surface area of the membrane and the driving force for permeation (the concentration gradient across the membrane wall) [2,3]. The total resistance to gas transfer consists of three terms, gas side resistance, liquid side resistance, and membrane resistance [2,9–11]. The gas side resistance is typically significantly smaller than that of the liquid side resistance. Furthermore, the mass transfer coefficient is independent of gas partial pressure, for partial pressures below 3 bar [1]. Thus with the membrane side resistance of a module being constant, the efficiency of the aeration process is most dependent on the liquid side resistance in submerged membrane bundles [1].

Previous research has highlighted the importance of module configuration and hollow fibre layout on the performance of various heat and mass transfer processes utilizing membrane modules [7,12–23]. Hollow fibre systems with parallel flow are often prone to flow mal-distribution with reduced flow through the centre of the fibre bundle. The water velocity increases radially culminating in preferential flow or channelling around the outside of the membrane bundle. This flow mal-distribution is

influenced by the module design (membrane diameter, length, packing density or inter-fibre spacing , bundle diameter, Reynolds number, bundle spacing, shell diameter, and possible dead zones caused flow around the potted ends of the module etc.) in a complex way that is poorly understood. Since the local velocity and shear flow determine the local mass transfer coefficient, the occurrence of such radial flow variation across the bundle results in lower overall rates of mass transfer and reduced reactor performance [17,24–26].

Many studies have been undertaken to understand and engineer the liquid flow field in membrane modules to enhance mass transfer [16,20,27–33]. Among applied methods, computational fluid dynamic (CFD) tools provide detailed analyses of the flow fields and the macro-scale diffusion of the species within the system, allowing for confident design and characterization of mass transfer within membrane bundles. Typically to reduce computational costs and time, single fibres or a section of the module geometry is modelled and simplifying assumption are applied [17,28,31,34–36]. Previous studies have utilized CFD modelling to, for example, predict the effects of operating parameters on the performance of various hollow fibre membrane processes [17,18,30,37]. The impact of module packing density on filtration efficiency, as well as fouling and cake growth, have been assessed using a finite element approach [38,39]. The results showed the significance of packing density on the flow distribution and filtration rate, with a 30% increase in membrane packing density leading to a 50% reduction in filtration flux.

In this paper we extend this approach to develop a validated CFD model of flow distribution in the modules followed by experimental gas transfer performance studies in order to better inform the analysis and design of hollow fibre modules. Flow distributions in different hollow-fibre modules, having different numbers of fibres and fibre spacings, were characterised experimentally using a tracer-response approach, and the residence time distribution (RTD) curves obtained were compared with those predicted by a CFD model; allowing validation of the CFD model. To evaluate the significance of the hydrodynamic conditions on the overall mass transfer performance, specific oxygen transfer rate (OTR) tests were performed with the same modules. The novelty of this research is the robust experimental validation of the CFD model, thus allowing for more confident assessment of the effect of

localised flow patterns in the module and subsequent analysis of the impact of these patters on gas-transfer performance.

2. Materials and Methods

2.1. Membrane Bundle Fabrication

Hollow fibre membrane modules typically consist of parallel fibres packed in an external shell. This provides a very large specific surface area for transfer. It has been shown that structured fibre configurations cause less flow mal-distribution and enhance mass transfer efficiencies [36,40,41]. In this study, homogeneous dense PDMS hollow fibre membranes were used. Fibre bundles were assembled using a predetermined hexagonal spacing, held in place by two plastic disk spacers on each end of the bundle. Details of the module designs are summarized in Figure 1 and Table 1.

Modules were fabricated with 4, 7, 19 and 37 fibres of the same length and assembled in 2mm, 4mm, and 6mm spacing configurations (due to design restrictions and the small column diameter, bundles of 19 fibres with 6mm spacing, and 37 fibres with 4 and 6 mm spacings, could not be tested). In all, nine fabricated bundles were used to study effects of geometry on hydrodynamics of the shell side flow and mass transfer efficiency.

The membrane bundles were potted into 6mm OD (4mm ID) polyethylene tubing at each end, using polyurethane potting agent (RS Components, Dublin Ireland). This potting material reduces the risks of gas or liquid leaks and can endure high pressures of up to 3 bar gauge. Spacers were placed at the ends of the bundle, keeping the effective fibre length of all fibres 42cm, from spacer to spacer. Each potted bundle was inserted in an 80cm vertical glass tube with an inner diameter of 25mm. Two stainless steel 6mm OD pipes held the bundle at a fixed vertical position (figure3) and provided the air flow to the membranes.

2.2. Computational Fluid Dynamics

The flow characteristics controlling the performance of hollow fibre membrane bundles were investigated numerically with a finite volume CFD method. The membrane bundle in the glass column was chosen as the computing domain. The three dimensional geometric structures of the computational domain were generated using Gambit 2.4 software which was then divided into smaller sub-domains. Hydrodynamic studies were carried out by developing a double precision model using the commercial software Fluent 6.3.26. Fluid properties were defined and appropriate boundary conditions were set. Velocity inlet and pressure outlet boundary conditions were set at the shell side inlet and outlet respectively. In order to conserve computational time and achieve correct results, grid sensitivity studies were conducted. Grids as small as 10% to 100% of the smallest dimension (0.5mm) were applied to the geometry to confirm that chosen grid sizes for each geometry resulted in grid-independent numerical results upon further grid refinement. A structured and fine mesh was applied to smaller and sensitive regions such as inter-fibre areas to confirm the accuracy of flow prediction in those areas. The amplified radial cross sections of the computational domain and grids are shown in Figure 2. More details on the mesh sizes are provided in Figure S1 and Table S1 in the supplementary information.

The flow field for all bundles was initially solved in steady state by SIMPLE coupling of the momentum and continuity equations for three water inlet velocities of 2.7, 4.8 and 6.9 cm/s. The flow field is solved as an incompressible, isothermal, steady state case. The continuity conservation equation is written as

$$\nabla.(\vec{v}) = 0 \qquad \text{Equation 1}$$

And the rate of change of momentum in each direction is as

$$\frac{\partial(\rho\vec{v})}{\partial t} + \nabla.(\rho\vec{v}\vec{v}) = -\nabla p + \nabla.(\bar{\bar{\tau}}) + \rho\vec{g} \qquad \text{Equation 2}$$

Where τ is the Reynolds stress tensor. A two equation turbulence model, standard k-ε model originally developed by Launder and Spalding 1974 [42], was used to predict the velocity profiles for the two higher inlet velocities, 2.7 and 4.8 as the flow is transient in these two cases (Reynolds numbers of 1335 and 1632 respectively) and

the flow is prone to larger local turbulent areas. The turbulent kinetic energy (k) equation and the rate of kinetic energy dissipation (ε) in each direction are solved as equation 3 and 4 respectively.

$$\rho\frac{\partial k}{\partial t}+\frac{\partial(\rho v_i k_i)}{\partial x_i}=\frac{\partial}{\partial x_i}\left((\mu+\frac{\mu_t}{\sigma_k})\frac{\partial k}{\partial x_i}\right)+G+B-\rho\varepsilon \qquad \text{Equation 3}$$

$$\rho\frac{\partial \varepsilon}{\partial t}+\frac{\partial}{\partial x_i}(\rho v_i \varepsilon)=\frac{\partial}{\partial x_i}\left((\mu+\frac{\mu_t}{\sigma_\varepsilon})\frac{\partial \varepsilon}{\partial x_i}\right)+C_1\frac{\varepsilon}{k}G+C_1(1-C_3)\frac{\varepsilon}{k}B-C_2\rho\frac{\varepsilon^2}{k} \qquad \text{Equation 4}$$

Where μ_t is the eddy viscosity, G is the rate of turbulent kinetic energy production and B is its rate of dissipation.

$$G=-\rho\overline{v_j' v_i'}\frac{\partial v_i}{\partial x_j}\approx \mu_t(\frac{\partial v_i}{\partial x_j}+\frac{\partial v_j}{\partial x_i})\frac{\partial v_i}{\partial x_j} \qquad \text{Equation 5}$$

$$B=\overline{\rho' v_j'}g_j\approx -\frac{\mu_t}{\rho\sigma_p}\frac{\partial \rho}{\partial x_j}g_j \qquad \text{Equation 6}$$

Where C_1=1.44, C_2=1.92, C_3=0.09, σ_p=1, σ_k=1.3.

To evaluate flow distribution and inter-fibre mixing in the column, a tracer was injected in the centre of the bundle. As well as incorporating unsteady state flow to follow tracer transport in time, a convection-diffusion equation is applied to model mass diffusion due to concentration (C) gradients and species transport due to convection

$$\frac{\partial(\rho C)}{\partial t}+\nabla.(\rho\vec{v}C)=-\nabla.\vec{J} \qquad \text{Equation 7}$$

Where $\vec{J}$ is the diffusion flux of tracer due to concentration gradient

$$\vec{J}=-\left(\rho D+\frac{\mu_t}{Sc_t}\right)\nabla \qquad \text{Equation 8}$$

Sc is the dimensionless Schmidt number. The second term in the brackets in equation 8 is neglected for laminar flow cases.

2.3. Tracer-Response Studies

A series of tracer injection experiments were conducted to evaluate the uniformity of the mixing and the presence of possible low velocity or dead zones leading to loss of mass transfer efficiency. In addition, these experiments were used to confirm the validity of CFD flow predictions.

To conduct the tracer-response experiments, an additional hollow fibre membrane was attached to the central fibre of the bundle to be used as the tracer injection fibre. The injection tip was fixed at 10cm above the lower spacer (Figure 3-right). The other end of the injection fibre was fitted with a luer lock fitting, allowing for the secure attachment of the injection syringe (Figure 3-right). Pictures of the actual experimental set up are provided in Figure S2 in the supplementary information. The positioning of this fibre in the centre of bundle cross section allowed for the injection of a tracer and following its dispersion along and among the fibres. The tracer injected can mimic the oxygen transferred from the central fibre to the liquid in the sense that it shows the extent of convection of water containing the transferred gas species at a certain time. Sustained high concentrations of the tracer within the bundle and poor dispersion to the bulk liquid is an indication, for example, of poor mixing and low velocity zones within the bundle cross section. Identifying regions of poor flow is of great importance, since, poor mixing results in higher local dissolved gas concentrations around the membranes and lower gas transfer rates.

Grade 1 pure water (18.2 MΩ cm^{-1}) obtained from an Elga Process Water System (Biopure 15 and Purelab flex 2, Veolia, Ireland) was pumped upflow through the column using an adjustable flow pump (Cole-Parmer, Fisher Scientific Ireland Ltd). The experimental set-up for the tracer study is illustrated on the right hand side of Figure 3.

Tracer studies were performed at three water inlet velocities in the column, 2.7, 4.8 and 6.9 cm/sec by injecting 0.02ml of 1M HCl solution through the injection fibre (highlighted in figure 3). The HCl solution was tinted with Methylene Blue for visual inspection. A conductivity probe (WTW inoLab, Wissenschaftlich Technische, Germany) was positioned in the centre of the tube, 15cm above the upper spacer, and perpendicular to the flow direction, to detect the temporal conductivity values of the water stream. Mesh spacers positioned above the column inlet and below the

conductivity probe, together with long downstream and upstream free spaces in the glass column, encouraged fully developed flow in the test section. The conductivity-time data were recorded using a data logger (PicoLog 1216 Data Logger - Pico Technology, Cambridgeshire, United Kingdom). Conductivity values were translated to HCl concentrations using a pre-obtained concentration-conductivity calibration curve.

A total of 27 experiments were run under described conditions. Experiments were repeated 5-10 times to ensure reproducibility. An example of a pulse injection response curve is shown in Figure 4.

One of the most commonly used models for describing the non-uniformity of streamlines and diagnosing poor flow is the RTD function analysis. It can be calculated according to the total mass of injection and the temporal concentration of the tracer.

$$E(t) = \frac{C(t)}{\int_0^\infty C(t)dt} \qquad \text{Equation 9}$$

The average species residence time, calculated by Equation 10, reflects the degree of mixing in a reactor. In the case of fully mixed flow, with no stagnant areas or dead zones, the mean residence time will be equal to the hydraulic residence time, which is calculated by dividing the reactor volume by the volumetric flow rate of the fluid.

$$t_m = \int_0^\infty tE(t) \qquad \text{Equation 10}$$

In many processes, longer residence times are more favourable. In these cases, larger deviations of mean residence time from the hydraulic residence time that are generally an indication of longer contact time, mean enhanced mass transfer [29]. However, in the case of submerged hollow fibre membranes, a longer residence time infers the existence of dead zones and stagnant areas. This non-uniformity in mixing might cause local oxygen concentration polarization, leading to local reductions in concentration gradients on the outside of the membranes, thus lower rates of oxygen transfer to the liquid. Mass transfer is improved if the flow is closer to a plug flow

reactor (symmetrical and sharp RTD curve). For a clear evaluation of the shape of the RTD curve, the RTD curve variance is also considered (Equation 11). Smaller variances indicate narrower RTD peaks, thus more uniform flows. To be able to compare results independent of their residence time, a dimensionless form of variance is used. Dimensionless variance is calculated as in Equation 12.

$$\sigma^2 = \int_0^\infty (t - t_m)^2 E(t) dt \qquad \text{Equation 11}$$

$$\sigma_D^2 = \frac{\sigma^2}{T_m 2} \qquad \text{Equation 12}$$

Furthermore, the skewness of the RTD curve is sometimes considered. It measures the extent to which the distribution is skewed to one side or another, meaning the asymmetry of the distribution (equation 13). Positive skewness indicates that the tail on the right side of the graph is longer while negative skewness suggests the opposite side of the graph is longer or fatter and the majority of the graph is concentrated on the right hand side of the graph. A symmetrical graph has zero skewness. The smaller the skewness value, the closer the flow is to a plug flow reactor.

$$S^3 = \frac{1}{\sigma^{3/2}} . \int_0^\infty (t - tm)^3 . E . dt \qquad \text{Equation 13}$$

2.4. Oxygen Transfer Experiments

Specific oxygen transfer rate experiments were performed to evaluate hydrodynamic effects on the gas transfer behaviour of membrane bundles. The column and the recirculation line were initially filled with tap water. The water was then deoxygenated by sparging the recirculated stream (circulation rate of 6.9cm/s) with pure nitrogen in the inline reservoir (Figure 3-left) until the DO reached as low as 0.07 mg/lit. Pure oxygen gas was introduced to the inside of the hollow fibres at a pressure of 50-100 mBarg and a minimum flow rate of 150ml/min, which was sufficient to maintain a constant partial pressure of oxygen within the fibres during the study. A dissolved oxygen (DO) probe (CellOx® 325, WTW Wissenschaftlich-Technische Werkstätten GmbH, Germany) was installed near the column outlet to measure the local dissolved oxygen concentration with time. Oxygen concentration

readings were collected using a Pico 1216 data logger. Dissolved oxygen concentrations were recorded as a function of time until the dissolved oxygen concentration in the recirculated liquid stream approached saturation. The temporal concentration values were used to calculate the rate of oxygen transferred to the liquid using a basic mass balance equation.

2.5. Empirical correlation between local velocity profiles and oxygen transfer efficiency

Mass transfer coefficients in hollow fibre membrane modules are often complex to describe as there are many contributing factors such as the module configuration, packing density, liquid inlet velocity and the shell side velocity distribution. Various studies have proposed empirical correlations to predict the mass transfer coefficient for different operating conditions [28,38,39,43–52]. These correlations, many of which were developed in lab-scale membrane modules are always effective in the prediction of the performance of larger, more practical modules, which are employed commercially. Table 2 shows some of the reported shell-side mass transfer correlations from the literature. The general form of the proposed correlations is as in equation 14.

$$\mathrm{Sh} = \mathrm{A}\,\mathrm{Re}^{\mathrm{x}}\,\mathrm{Sc}^{\mathrm{y}} \qquad \text{Equation 14}$$

Where A is a constant and the Sherwood, Schmidt and Reynolds numbers are calculated as $Sh=Kd_{eff}/D$, $Sc=\mu/D\rho$, $Re=\rho u d_{eff}/\mu$ respectively, and d_{eff} is the effective diameter of the column. The module effective diameter is calculated as

$$\mathrm{d_{eff}} = \frac{(\mathrm{d_{bundle}}^2 - \mathrm{n d_{fibre}}^2)}{(\mathrm{d_{bundle}} + \mathrm{n d_{fibre}})} \qquad \text{Equation 15}$$

Where d_{bundle} is the cross-sectional diameter occupied by fibres, n is the number of fibres and d_{fibre} is the outer diameter of the membrane fibres. More information on the calculation of d_{bundle} is provided in table S4 in the supplementary information.

The power x is the indication of the extent of velocity dependence of the mass transfer. It has been reported to be within a range of 0.3-0.93 in various studies in

the literature, mainly depending on the range of Reynolds calculated from the inlet velocity.

In these studies, apart from module inlet velocity, the packing density is the primary controlling factor in the rate of transfer. If localised velocity distributions (obtained from the CFD model) for each module configuration are utilized instead of inlet velocity, the packing density can removed as its contribution is incorporated intrinsically in the velocity profile.

Previous studies have oftern employed correlations that use Reynolds number estimates based on the inlet velocity. As shown previously the local velocity values have a profound impact on boundary layer thickness and the mass transfer coefficient, which directly influences the aeration efficiency [31]. However, unlike previous studies, where a uniform average velocity across the module cross-sectional area was used, here, the average velocity within the hollow-fiber bundle (the space occupied by hollow fibres) is utilised. For all computational cells existing in the cylindrical region occupied by the hollow fibre membranes, with radius of r_{bundle} and length of the fibres (42cm), local velocities are extracted and the bundle region average velocity is obtained. More information on the cylindrical area of focus and r_{bundle} of different hollow fibre configurations are provided in the supplementary information table S4. The bundle area average velocity is used to calculate effective Reynolds numbers for all bundles of study at various inlet velocities. The diameter of the bundle area is also used as the effective diameter when calculating corresponding Reynolds numbers. Schmidt number is independent of the fiber number or spacing employed in the modules and is the same for all operating conditions and module configurations. The exponent y in Equation 14, is typically 0.33 in the literature and the same value is assumed here. The calculation of exponent x requires comparisons of the right hand side of the equation with a previously obtained and confirmed Sherwood number on the left hand side of the equation, i.e., experimentally calculated Sherwood number for each bundle.

3. Results and discussion

3.1. Flow mixing (assessed by CFD)

The shell side flow field was numerically solved at three inlet velocities for all bundles of study using the FLUENT CFD code. The power of using a validated CFD model is the access to features of shell-side hydrodynamics, particularly when there may be geometric features (for example, spacers) in the modules that are significant enough to affect the hydrodynamics. A sample of the velocity contour plots is presented in figure S3 in the supplementary information. As expected, the results show that, at the higher membrane packing densities (smaller spacings), the inter-fibre velocity was significantly lower than the bulk liquid velocity. (The term “bulk liquid” refers to liquid outside of the fiber bundle). At higher packing densities the boundary layers surrounding each fiber impose a greater effect on the flow within the bundle, which slows the local velocity and encourages preferential flow around the outside of the membrane bundle (see Figure S3 in supplementary information).

Water flows parallel to the hollow fibers, with small disturbances in the axial flow mainly around the spacers bounding the membrane module. Comparisons between the axial and radial velocities plotted in Figures S4 to S6 in the supplementary information shows that the flow disturbance caused by the spacers occurs in a larger area for higher inlet velocities and dampens more quickly in lower velocities. At an inlet velocity of 2.7cm/s the flow is laminar with an average 0.015% probability of local turbulence in the column. This probability increases to between 5 and 20 percent for water velocities of 4.8 and 6.9 cm/s respectively. Further details on local Reynolds numbers are provided in Table S2 in the supplementary information section.

The transport of an inert tracer was simulated using CFD for the same set of conditions under which experimental tracer experiments were conducted, and the results were then used to validate the CFD model. The time-dependent tracer response curves were compared for all packing densities and inlet velocities. Representative data for a water inlet velocity of 6.9 cm/s are shown in figure 5. It is clear that there is a good agreement between the experimental and modelled response curves, which validates the use of the CFD model to further analyze the hydrodynamics in the hollow fibre configuration.

The experimental curves in Figure 5 represent the averages of 8 to 12 runs for each membrane configuration. The shape of the tracer response curves provides insight into the flow patterns. A pulse injection in a plug flow reactor will result in a sharp and narrow peak in the effluent concentration profile. Therefore, wide curves suggest deviation from plug flow behaviour. Long tailing of the curve is an indication of the flow straying from the Gaussian distribution thus deviating from uniform velocity distribution across the membrane bundle. Larger bundles show a larger extent of deviation from uniform flow.

Flow distribution significantly changes with varying fibre spacing as well as bundle to annulus radius ratio. Among the bundles tested, those with sharp peaks and a normal distribution are at an optimum from a mass transfer perspective as they provide a more uniform flow distribution, better mixing and reduce the chance of local concentration polarization.

For both experimental and simulation data, the mean residence times for all 9 configurations were calculated using equation 10. To assure model validity, these comparisons are shown in Figure 6 where it can be seen that there is satisfactory agreement between the CFD model predictions and experimental data.

3.2. Tracer-Response Distribution analysis

As the tracer was injected adjacent to the central fibre, it was transported through the fibre bundle into the bulk liquid and to the conductivity meter. Experimentally obtained time dependent tracer response data were used to prepare residence time distribution (RTD) curves which allow the calculation of mean residence time (t_m) and response curve variances (σ_D) using equations 10-12 for each bundle configuration. Figure 7 summarises this data for all membrane configurations and for a range of fibre inlet velocities, (2.7, 4.8 and 6.9 cm/s). The hydraulic residence times ($\bar{t}$) for the applied water velocities are calculated as 16.4, 9.2 and 6.3s respectively.

As expected, the mean residence time decreases with increasing liquid velocities for all bundle configurations. However a definite trend cannot be observed when it comes to the number of fibres present or fiber spacing. The velocity field changes

with inlet velocity even for the same module. At higher inlet velocities, i.e. transitional flow, larger regions of turbulence influence the dispersion of the tracer. The resulting complex flow paths increase the chance of secondary flows that influence the behaviour of the bundle. Hence, the overall trends are similar for the experiments performed at 4.8m/s and 6.9 m/s, while the same bundles show different trends at lower inlet velocities. In both transitional flows, the 7 fibre bundle with 6mm spacing has the lowest residence time and the 37 fibre bundle with 2mm spacing has the highest residence time. For ease of comparison, the variance and skewness of the RTD curves for all bundles tested are depicted in Figure 7-right. The skewness of the curves is stacked on top of the variance in a lighter colour for ease of comparison.

The variance shows similar trends to the mean residence times for bundles tested at the same inlet velocity; the spread of the tracer peak becomes smaller as the water velocity increases and residence time drops. Non-zero skewness of the curves is an indication of deviation from plug flow. Generally the skewness of the graphs decrease with velocity and are very smaller than the variances of the curves. Smaller skewness and variance of the curves is an indication of better mixing in the column and uniform flow field. Although at higher velocities these indexes are smaller, the same trend is not observed when increasing fibre spacing. Due to the complexity in these observations, a conclusion on the optimal bundle configuration is only possible by directly assessing the velocity field. Fundamental studies of the velocity distribution in the cross section of the column can provide valuable information, which helps to explain this behaviour.

3.3. Specific oxygen transfer rate prediction

The CFD model provides the basis for a more in-depth analysis of the water velocity distribution in the membrane module. An example of local velocity profiles for modules employed in this study are shown in figures S7 and S8 in the supplementary information. The velocity profiles clearly show, lower water velocities within the fiber bundles compared to the bulk liquid, and the drop is more marked as the inter-fiber spacing decreases.

Many studies base their mass transfer performance evaluations on the liquid inlet velocity or an average shell-side velocity, an approach which neglects the effect of

geometric features within the modules that may influence hydrodynamics. However the use of a validated CFD simulation, allows the flow field within the bundles to provide more information when assessing mass transfer performance. Here, the velocity profiles for the different membrane modules are utilized to help predict the specific oxygen transfer rates in those bundles. In an attempt to compare CFD predictions with the correlations in the literature, the general form of equation 14 is utilized. The model Sherwood number is calculated for all investigated cases, different membrane configurations and inlet velocities, by incorporating the bundle area average velocities and the bundle area diameter in the right hand side of equation 14 as previously explained in section 2.5. Exponents x and y are to be obtained by comparing model predicted Sherwood numbers with the values experimentally measured.

To obtain the experimental Sherwood numbers, the shell-side mass transfer coefficient (K) is required. Thus, OTR tests were performed for all 9 bundles at three inlet velocities. Fibre bundles of 2mm spacing were twisted to mimic zero spacing bundles with adjacent fibres touching. Experiments were repeated to confirm reproducibility. The water recirculation rate was fixed at 12.3, 21.8 and 31 ml/min for the three inlet velocities of 2.7, 4.8 and 6.9 cm/s respectively. OTR results for the studied fibre arrays at the highest inlet velocity are presented in Figure 8.

The results show an average decrease in the specific rate of oxygen transfer with an increasing number of fibres in a bundle. As expected, bundles with no spacing between the fibres have the lowest overall transfer of oxygen compared to loosely packed bundles, where a 2mm increase in spacing can lead to up to two-fold improvement in the performance. However, further increases in the spacing seem to have diverse effects on the aeration rate. The OTR rises only by 3% for the 19 fibre bundle when increasing the intra-fibre spacing from 2mm to 4mm. The 7 fibre bundle transfers 8% less oxygen when put together with 6mm spacing rather than 4mm, while the same procedure reduces the OTR for the 4 fibre bundle by almost 3%.

The experimental mass transfer coefficient, and therefore the experimental Sherwood number is calculated from the temporal dissolved oxygen concentration data from the OTR experiments. As the Sc number is constant, $Sh/Sc^{0.33}$ is plotted

against the Reynolds number calculated from CFD model velocity profiles, on a log-log axis to quantify their exponential relationship (figure9).
The constant A is calculated from the intercept of these graphs. With A and exponents x and y determined, equation 16 is proposed to predict oxygen transfer coefficient using CFD model velocity profile results.

$Sh=1.7Re^{0.42}Sc^{0.33}$ Equation 15

The proposed correlation is used to calculate the CFD model Sherwood numbers. Experimental and model-calculated Sherwood numbers are compared in figure 10. The results show satisfactory predictions using the CFD model local velocity data, with an R^2 value of 0.71 over the entire range, with approximately 70% of the cases computationally predicted being within 20% error margin of the experimental data. The previously proposed correlations suggest that the Reynolds number power index for laminar flow is close to 0.33 [45–47,50]. In this study, the x power index is found to be slightly higher which would suggest the presence of local turbulent areas. In the case of turbulent flow, the velocity dependence of the mass transfer rate is more significant with an exponent of 0.5-0.9.[28].
The proposed correlation in this study has been compared with some of the previous correlations from the literature (Table 2). For a wider overview, comparisons were made even if the operating range suggested by the authors do not match the range tested in this study. For a comprehensive comparison, different approaches were taken.
In the first approach, to calculate the Sherwood number using literature correlations, the Reynolds number was calculated using the local velocity values obtained from CFD and the proposed module packing densities and effective diameter of d_{Bundle} (table S4 in the supplementary information) were plugged in where required.

The same technique was applied in approach 2, with a difference in the way the packing density is calculated. In this approach, the packing density is calculated as proposed by the referred studies, using the following equation (eq16).

$$\varphi = \text{number of fibres} \times \left(\frac{d_{\text{fibre}}}{d_{\text{Column}}}\right)^2 \quad \text{Equation 16}$$

In the third and final approach, the nominal Reynolds numbers was calculated based on the shell inlet velocity as proposed by majority of the published studies. The same packing density employed in approach 2 was utilized.

For each of the previously proposed correlations and each of the approaches, the percentage error between correlation-calculated and experimental Sherwood numbers for each module and each inlet velocity (27 cases total) was calculated using equation 17.

$$\% \text{ Error} = 100 \times \frac{|\text{Correlation Sh} - \text{Experimental Sh}|}{\text{Experimental Sh}} \qquad \text{Equation 17}$$

The average and standard deviation of the percentage error over all 27 cases are reported in table 2. Comparing the error percentages, it is apparent that the correlation proposed here is the best fit to the experimental data of this study.

4. Conclusion

A CFD model was used to study the hydrodynamics in a hollow-fiber membrane contactor with variable fibre numbers, spacing and liquid flow velocities. Unique tracer-response experiments were performed to characterize the fluid flow behaviour and was also used to successfully validate the CFD model by comparing tracer-response curves. Several factors were found to influence the flow pattern, such as the fibre bundle to annulus cross-sectional areas, the number of membranes in the bundle and the fibre spacing and orientation. No general overall conclusions can be drawn for any of these influencing parameters without taking into account the effect on the other influencing parameters. Using the validated model, the shell-side velocity profiles were extensively studied and used to test a hypothesis regarding the relationship between flow distribution uniformity and specific oxygen transfer rates. Using predicted velocity profiles in the module shell, a correlation was proposed for the overall mass transfer coefficient using local velocity values for calculating Reynolds numbers. In addition, the gas transfer performance was evaluated experimentally and related to the hydrodynamic patterns. Increasing the fibre

spacing did not result in an increase in specific OTR in all cases as the wall effects greatly interfered with the velocity distribution in the inter-fibre areas as well as the bulk of the liquid. Good agreement was obtained between model-calculated and experimental Sherwood numbers. Previously published correlations for membrane contactors are generally system specific. This limitation can be overcome by employing CFD, which provides a number of benefits including analysis of localised hydrodynamic effects within complex geometries and the ability to optimise the design membrane modules in a less time-consuming manner than experimental tests.

Acknowledgment

This research was supported by the Irish Research Council ‘Embark Initiative’.

Nomenclature

v	Velocity	m/s
ρ	Fluid density	kg/m^3
t	Time	sec
μ	viscosity	kg/m.s
k	Turbulent Kinetic Energy	m^2/s^2
ε	Turbulence dissipation	m^2/s^3
x	Length characteristic	m
D	Diffusion coefficient	m^2/s
C	Species concentration	g/l
Sc	Schmidt number	Dimensionless
Sh	Sherwood number	Dimensionless
K	Mass transfer coefficient	m/s
L	Effective length	m
r	Bundle area radius	m
R	Column ID	m
φ	Packing density	Dimensionless
D_{Column}	Column inner diameter	m
d_h	Hydraulic diameter	m
d_{eff}	Effective diameter	m
d_{fibre}	Fibre outer diameter	m

References

[1] P. Côté, J.-L. Bersillon, A. Huyard, Bubble-free aeration using membranes: mass transfer analysis, J. Memb. Sci. 47 (1989) 91–106.

[2] P. Côté, J. Bersillon, A. Huyard, G. Faup, C. Pierre, Bubble-Free Aeration Using Membranes : Process Analysis, J Water Pollut Control Fed. 60 (1992) 1986–1992.

[3] T. Ahmed, M.J. Semmens, The use of independently sealed microporous hollow fiber membranes for oxygenation of water: model development, J. Memb. Sci. 69 (1992) 11–20.

[4] M. Pankhania, T. Stephenson, M.J. Semmens, Hollow fibre bioreactor for wastewater treatment using bubbleless membrane aeration, Water Res. 28 (1994) 2233–2236.

[5] M.J. Semmens, K. Dahm, J. Shanahan, A. Christianson, COD and nitrogen removal by biofilms growing on gas permeable membranes., Water Res. 37 (2003) 4343–50.

[6] T. Ahmed, M.J. Semmens, M.A. Voss, Oxygen transfer characteristics of hollow-fiber, composite membranes, Adv. Environ. Res. 8 (2004) 637–646.

[7] A. Ahmadimotlagh, V. Voller, M. Semmens, Advective flow through membrane-aerated biofilms: Modeling results, J. Memb. Sci. 273 (2006) 143–151.

[8] M.J. Semmens, Alternative MBR configurations: using membranes for gas transfer, Desalination. 231 (2008) 236–242.

[9] M. Mavroudi, S.P. Kaldis, G.P. Sakellaropoulos, A study of mass transfer resistance in membrane gas–liquid contacting processes, J. Memb. Sci. 272 (2006) 103–115.

[10] N. Xu, S. Li, W. Jin, J. Shi, Y.S. Lin, Experimental and modeling study on tubular dense membranes for oxygen permeation, AIChE J. 45 (1999) 2519–2526.

[11] T. Ahmed, M.J. Semmens, Use of sealed end hollow fibers for bubbleless membrane aeration: experimental studies, J. Memb. Sci. 69 (1992) 1–10.

[12] A. Ali, P. Aimar, E. Drioli, Effect of module design and flow patterns on performance of membrane distillation process, Chem. Eng. J. 277 (2015) 368–377.

[13] T. Femmer, A.J.C. Kuehne, M. Wessling, Estimation of the structure dependent performance of 3-D rapid prototyped membranes, Chem. Eng. J. 273 (2015) 438–445.

[14] D.W. Johnson, M.J. Semmens, J.S. Gulliver, Diffusive transport across unconfined hollow fiber membranes, J. Memb. Sci. 128 (1997) 67–81.

[15] J. Wu, Shell-side mass transfer performance of randomly packed hollow fiber modules, J. Memb. Sci. 172 (2000) 59–74.

[16] X. Yang, R. Wang, A.G. Fane, Novel designs for improving the performance of hollow fiber membrane distillation modules, J. Memb. Sci. 384 (2011) 52–62.

[17] Z.-X. Li, L.-Z. Zhang, Flow maldistribution and performance deteriorations in a counter flow hollow fiber membrane module for air humidification/dehumidification, Int. J. Heat Mass Transf. 74 (2014) 421–430.

[18] E. Casey, Simulation studies of process scale membrane aerated biofilm reactor configurations, 4th International Water Association (IWA) Membranes Conference, Harrogate, UK, January, 2007. .

[19] S.S. Paul, M.F. Tachie, S.J. Ormiston, Experimental study of turbulent cross-flow in a staggered tube bundle using particle image velocimetry, Int. J. Heat Fluid Flow. 28 (2007) 441–453.

[20] L.-Z. Zhang, S.-M. Huang, W.-B. Zhang, Turbulent heat and mass transfer across a hollow fiber membrane bundle considering interactions between neighboring fibers, Int. J. Heat Mass Transf. 64 (2013) 162–172.

[21] X. Yang, E.O. Fridjonsson, M.L. Johns, R. Wang, A.G. Fane, A non-invasive study of flow dynamics in membrane distillation hollow fiber modules using low-field nuclear magnetic resonance imaging (MRI), J. Memb. Sci. 451 (2014) 46–54.

[22] S.-M. Huang, M. Yang, W.-F. Zhong, Y. Xu, Conjugate transport phenomena in a counter flow hollow fiber membrane tube bank: Effects of the fiber-to-fiber interactions, J. Memb. Sci. 442 (2013) 8–17.

[23] S. Rishell, E. Casey, B. Glennon, G. Hamer, Mass transfer analysis of a membrane aerated reactor, Biochem. Eng. J. 18 (2004) 159–167.

[24] A. Gabelman, S.-T. Hwang, Hollow fiber membrane contactors, J. Memb. Sci. 159 (1999) 61–106.

[25] V. Dindore, D. Brilman, G. Versteeg, Modelling of cross-flow membrane contactors: Mass transfer with chemical reactions, J. Memb. Sci. 255 (2005) 275–289.

[26] K.L. Wang, E.L. Cussler, Baffled membrane modules made with hollow fiber fabric, J. Memb. Sci. 85 (1993) 265–278.

[27] M.M. Teoh, S. Bonyadi, T.S. Chung, Investigation of different hollow fiber module designs for flux enhancement in the membrane distillation process, J. Memb. Sci. 311 fiber membrane distillation modules, J. Memb. Sci. 384 (2011) 52–62. (2008) 371–379.

[28] J. Wu, V. Chen, Shell-side mass transfer performance of randomly packed hollow fiber modules, J. Memb. Sci. 172 (2000) 59–74.

[29] X. Yang, R. Wang, A.G. Fane, Novel designs for improving the performance of hollow fiber Membrane distillation modules. J of Memb. Sci. 384 (2011): 52–62

[30] X. Yang, H. Yu, R. Wang, A.G. Fane, Optimization of microstructured hollow fiber design for membrane distillation applications using CFD modeling, J. Memb. Sci. 421-422 (2012) 258–270.

[31] L.-Z. Zhang, Z.-X. Li, Convective mass transfer and pressure drop correlations for cross-flow structured hollow fiber membrane bundles under low Reynolds numbers but with turbulent flow behaviors, J. Memb. Sci. 434 (2013) 65–73.

[32] H. Tabesh, G. Amoabediny, A. Poorkhalil, A. Khachab, A. Kashefi, K. Mottaghy, A theoretical model for evaluation of the design of a hollow-fiber membrane oxygenator, J. Artif. Organs. 15 (2012) 347–356.

[33] X. Yang, H. Yu, R. Wang, A.G. Fane, Analysis of the effect of turbulence promoters in hollow fiber membrane distillation modules by computational fluid dynamic (CFD) simulations, J. Memb. Sci. 415-416 (2012) 758–769.

[34] Y. Le Moullec, O. Potier, C. Gentric, J. Pierre Leclerc, Flow field and residence time distribution simulation of a cross-flow gas–liquid wastewater treatment reactor using CFD, Chem. Eng. Sci. 63 (2008) 2436–2449.

[35] J. Günther, P. Schmitz, C. Albasi, C. Lafforgue, A numerical approach to study the impact of packing density on fluid flow distribution in hollow fiber module, J. Memb. Sci. 348 (2010) 277–286.

[36] J. Günther, D. Hobbs, C. Albasi, C. Lafforgue, A. Cockx, P. Schmitz, Modeling the effect of packing density on filtration performances in hollow fiber microfiltration module: A spatial study of cake growth, J. Memb. Sci. 389 (2012) 126–136.

[37] M. Rezakazemi, Z. Niazi, M. Mirfendereski, S. Shirazian, T. Mohammadi, A. Pak, CFD simulation of natural gas sweetening in a gas–liquid hollow-fiber membrane contactor, Chem. Eng. J. 168 (2011) 1217–1226.

[38] Y. Wang, M. Brannock, S. Cox, G. Leslie, CFD simulations of membrane filtration zone in a submerged hollow fibre membrane bioreactor using a porous media approach, J. Memb. Sci. 363 (2010) 57–66.

[39] S.S. Paul, S.J. Ormiston, M.F. Tachie, Experimental and numerical investigation of turbulent cross-flow in a staggered tube bundle, Int. J. Heat Fluid Flow. 29 (2008) 387–414.

[40] L.-Z. Zhang, Heat and mass transfer in a randomly packed hollow fiber membrane module: A fractal model approach, Int. J. Heat Mass Transf. 54 (2011) 2921–2931.

[41] V.Y. Dindore, G.F. Versteeg, Gas–liquid mass transfer in a cross-flow hollow fiber module: Analytical model and experimental validation, Int. J. Heat Mass Transf. 48 (2005) 3352–3362.

[42] B.E. Launder, D.B. Spalding, The numerical computation of turbulent flows, Comput. Methods Appl. Mech. Eng. 3 (1974) 269–289.

[43] R. Thanedgunbaworn, R. Jiraratananon, M.H. Nguyen, Shell-side mass transfer of hollow fibre modules in osmotic distillation process, J. Memb. Sci. 290 (2007) 105–113.

[44] S. Shen, S.E. Kentish, G.W. Stevens, Shell-Side Mass-Transfer Performance in Hollow-Fiber Membrane Contactors, Solvent Extr. Ion Exch. 28 (2010) 817–844.

[45] A.G. Asimakopoulou, A.J. Karabelas, Mass transfer in liquid–liquid membrane-based extraction at small fiber packing fractions, J. Memb. Sci. 271 (2006) 151–162.

[46] A. ASIMAKOPOULOU, A. KARABELAS, A study of mass transfer in hollow-fiber membrane contactors—The effect of fiber packing fraction, J. Memb. Sci. 282 (2006) 430–441.

[47] S. Kartohardjono, 1, & V. Chen, Mass Transfer and Fluid Hydrodynamics in Sealed End Hydrophobic Hollow Fiber Membrane Gas-liquid Contactors, J. Appl. Membr. Sci. Technol. 2 (2005).

[48] A. Mansourizadeh, F. Ismail, Hollow fiber gas-liquid membrane contactors for acid gas capture: a review., J. Hazard. Mater. 171 (2009) 38–53.

[49] S.J. Lue, S.F. Wang, L.D. Wang, W.W. Chen, K.-M. Du, S.Y. Wu, Diffusion of multicomponent vapors in a poly(dimethyl siloxane) membrane, Desalination. 233 (2008) 277–285.

[50] M.J. Costello, A.G. Fane, P.A. Hogan, R.W. Schofield, The effect of shell side hydrodynamics on the performance of axial flow hollow fibre modules, J. Memb. Sci. 80 (1993) 1–11.

[51] S.R. Wickramasinghe, M.J. Semmens, E.L. Cussler, Hollow fiber modules made with hollow fiber fabric, J. Memb. Sci. 84 (1993) 1–14.

[52] M.C. Yang, E.L. Cussler, Designing hollow-fiber contactors, AIChE J. 32 (1986) 1910–1916.

Figure legends

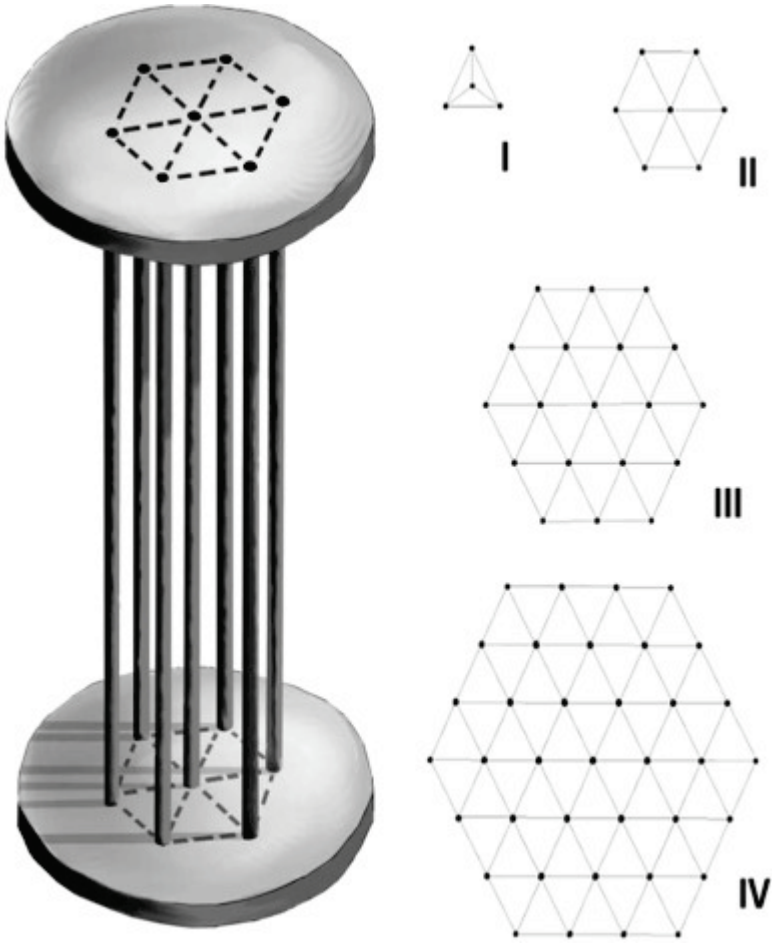

Figure 1 - Left - Schematic of a sample fibre bundle, Right- The hexagonal fibre orientation with I) 4, II) 7, II) 19 and IV) 37 fibres

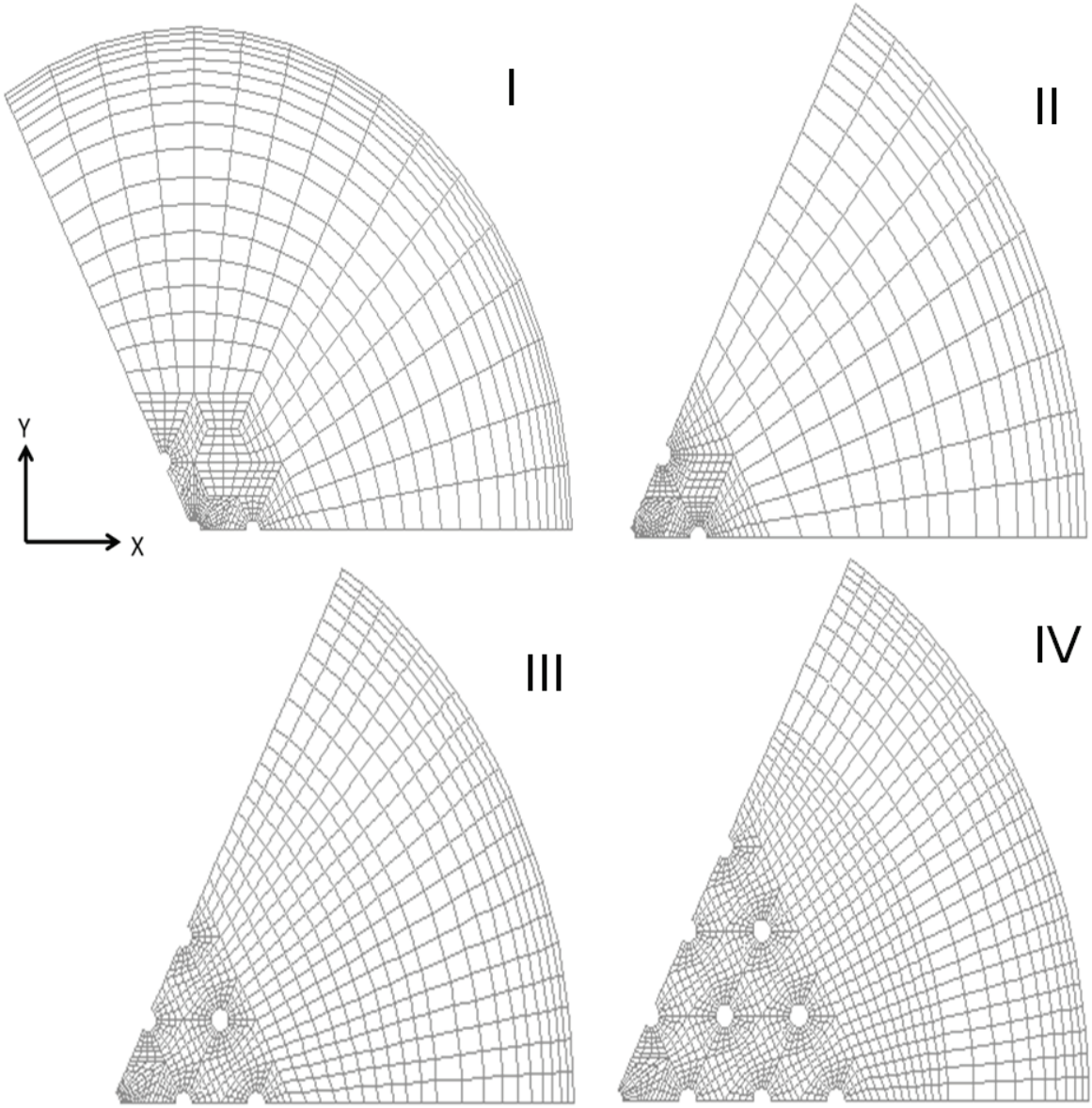

Figure 2- Cross sectional image of the computational domain I) 4, II) 7, II) 19 and IV) 37 fibres

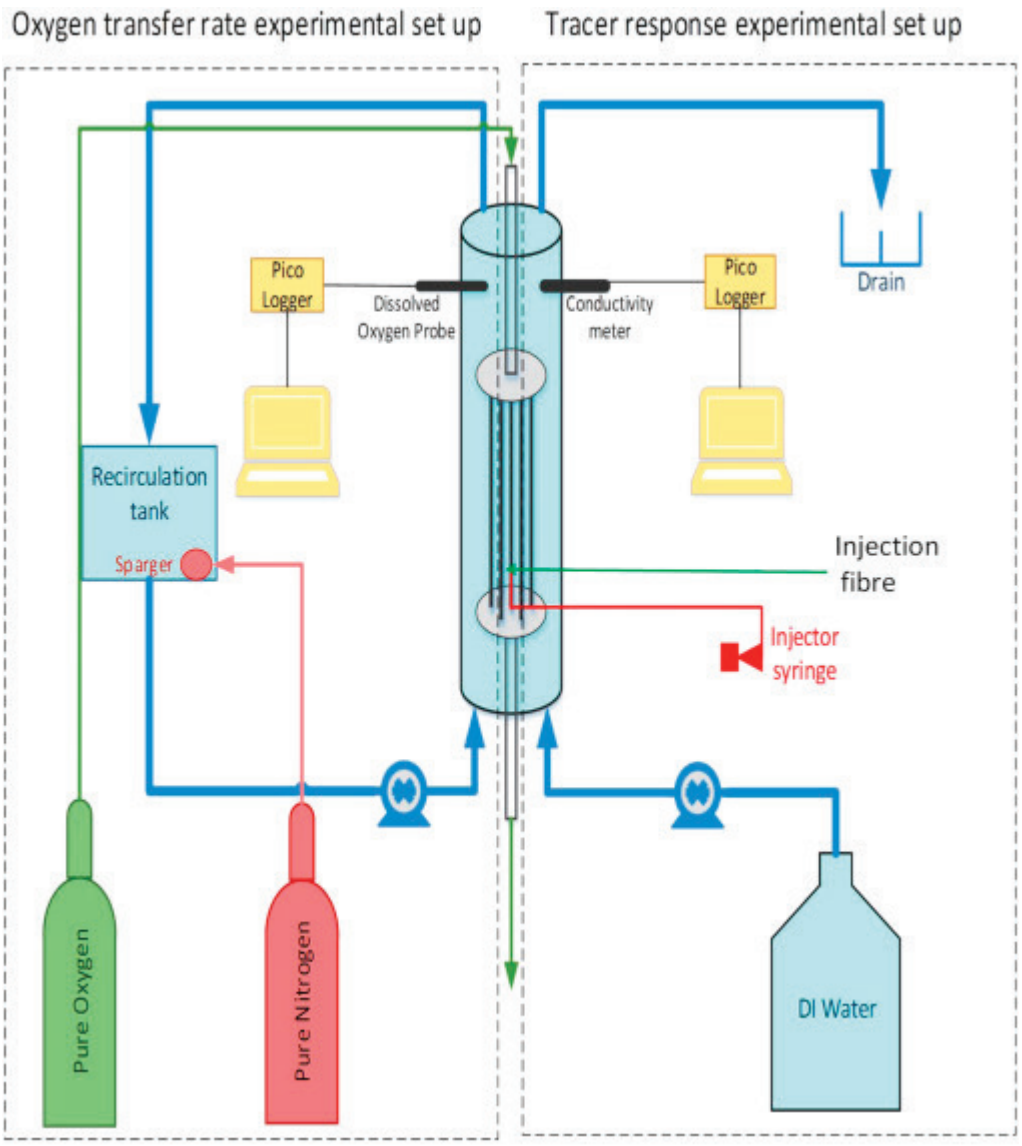

Figure 3- Schematic of the tracer response and specific oxygen transfer rate experimental set-ups

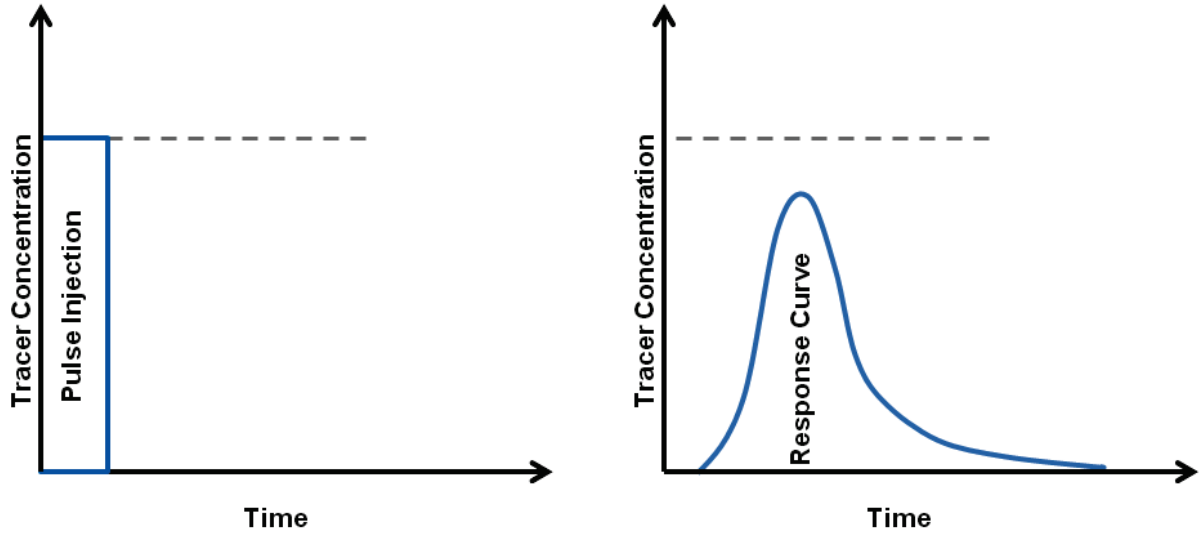

Figure 4- Tracer concentration vs. time for pulse injection, left-pulse injection, right-response curve

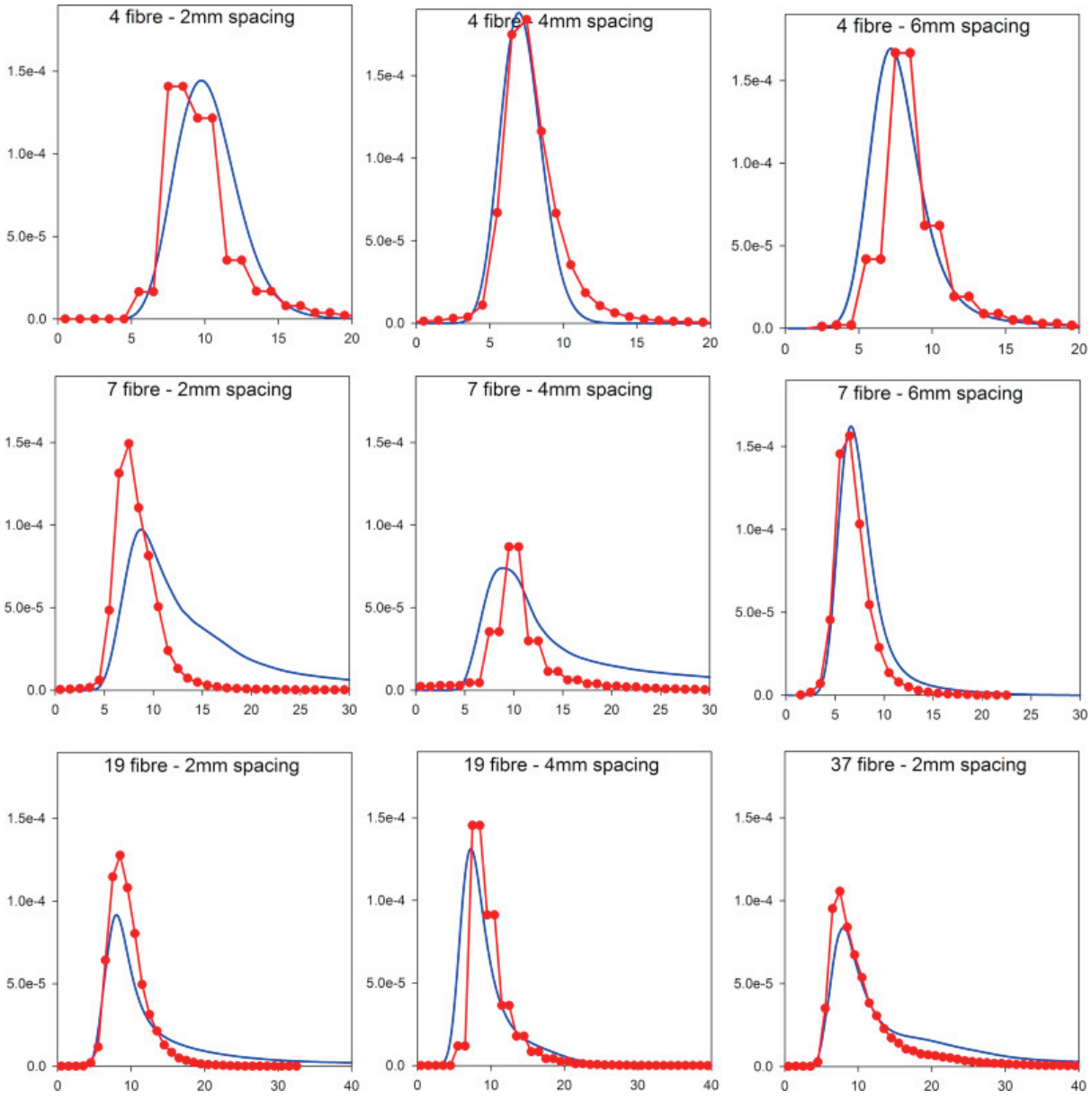

Figure 5 – Experimental and modelled tracer concentration for various bundle configurations at water inlet velocity of 6.9cm/s, y-axis: tracer molar concentration (mol/lit), x-axis: time (sec)

model, experimental data

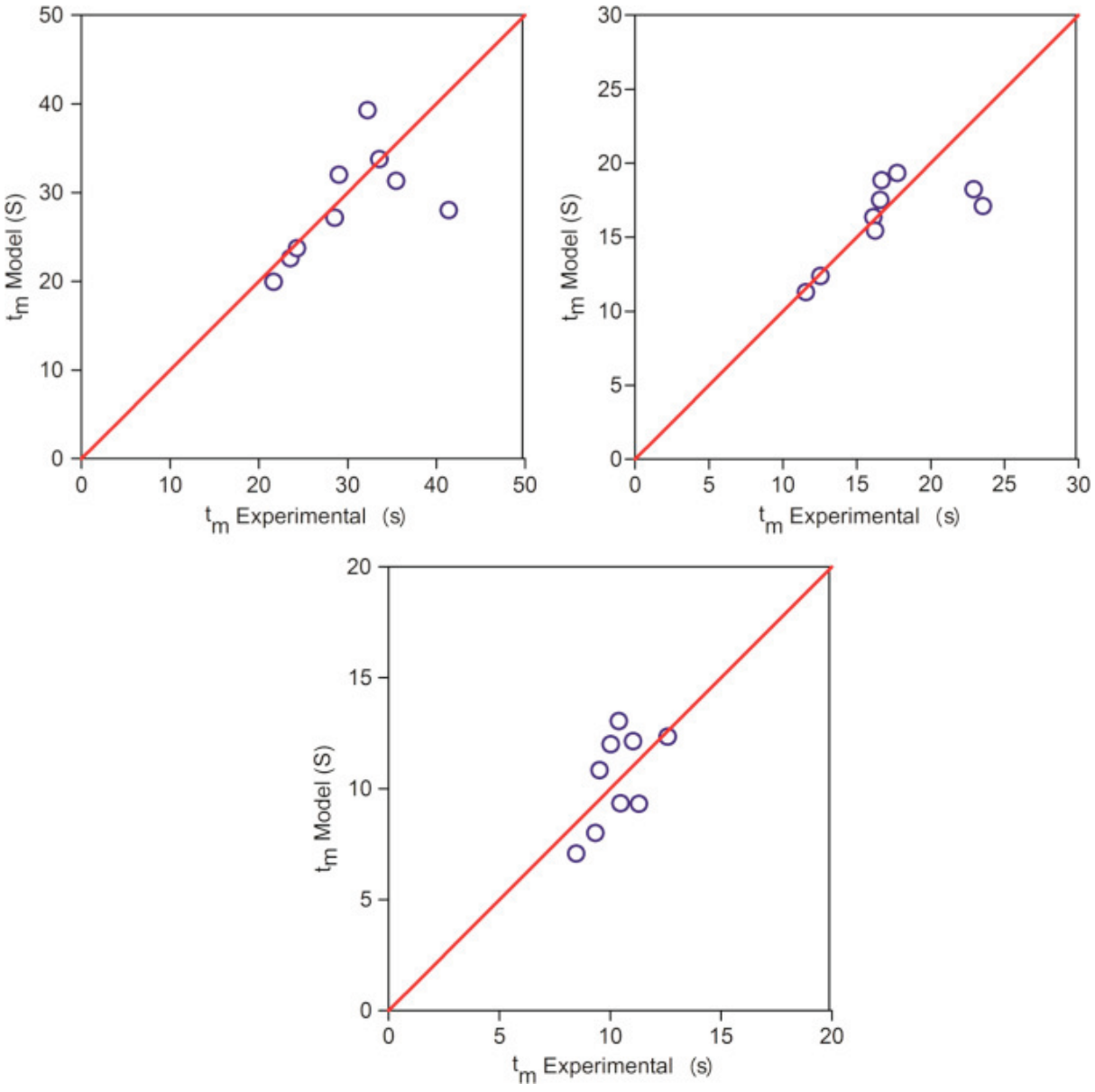

Figure 6 – Model and experimental mean residence time comparison for all bundle configurations, at inlet velocity of a) 2.7cm/s, b) 4.8cm/s, c) 6.9cm/s

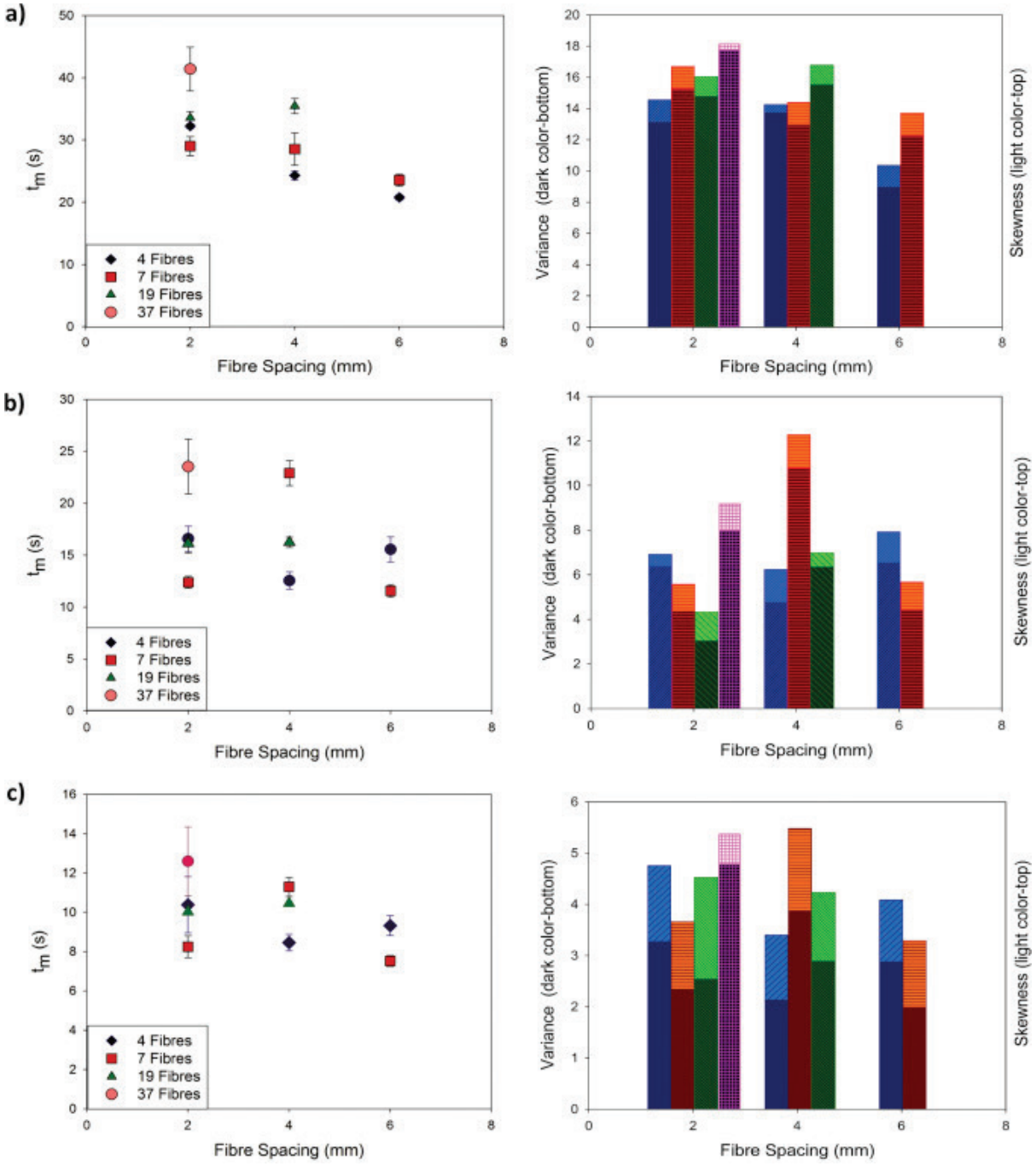

Figure 7- Experimental Mean residence time (left) and dimensionless variances (right) for various bundle configurations at inlet water velocities of a)2.7cm/s, b)4.8cm/s, c)6.9cm/s

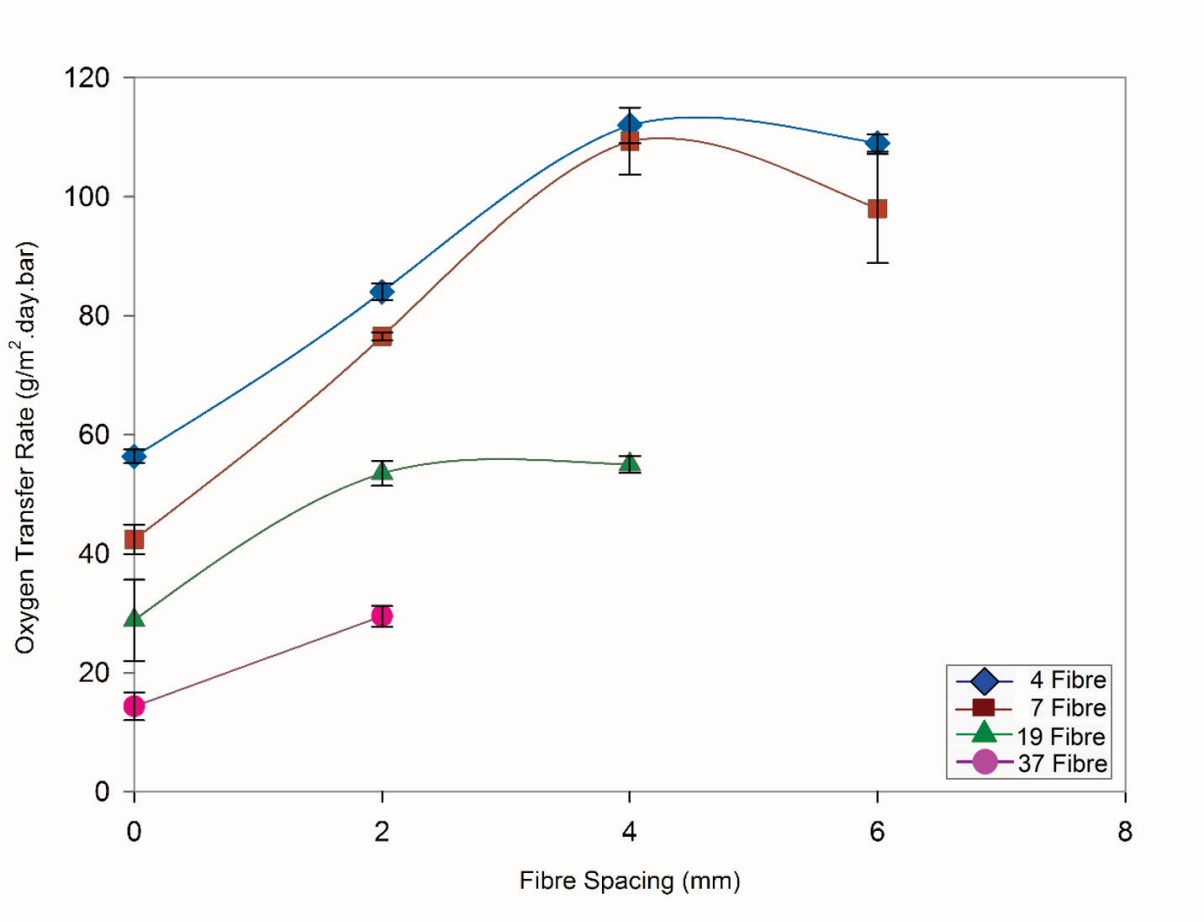

Figure 8- Specific oxygen transfer rate for bundles of 4, 7, 19, 37 fibres with fibre spacings of 2, 4 & 6mm at water inlet velocity of 6.9cm/s

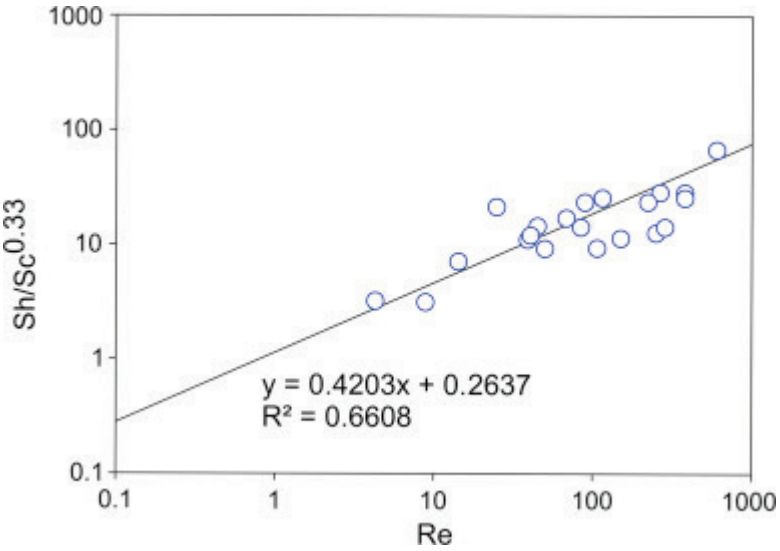

Figure 9- Relationship between ($Sh/Sc^{0.33}$) and Re for inlet velocities of a) 2.7cm/s, b) 4.8cm/s, c) 6.9cm/s

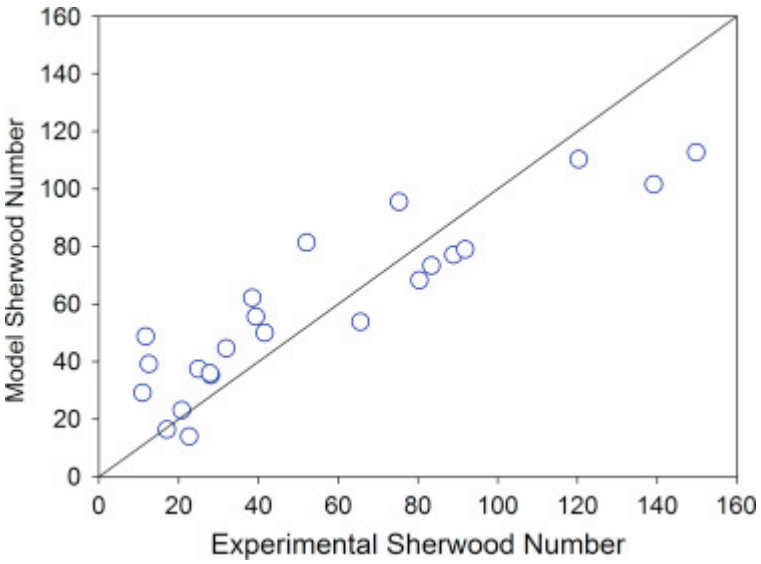

Figure 10- Model vs. experimental Sherwood numbers, a) Re=690, b) Re=1335, c) Re=1632